

ARTICLE OPEN



Age-dependent cortical overconnectivity in Shank3 mice is reversed by anesthesia

Elena Montagni^{1,2} , Manuel Ambrosone^{1,2,3} , Alessandra Martello^{1,3,4}, Lorenzo Curti⁵, Federica Polverini⁶, Laura Baroncelli^{1,7}, Guido Mannaioni⁵, Francesco Saverio Pavone^{2,3,8}, Alessio Masi⁵ and Anna Letizia Allegra Mascaro^{1,2,3} 

© The Author(s) 2025

Growing evidence points to brain network dysfunction as a central neurobiological basis for autism spectrum disorders (ASDs). As a result, studies on Functional Connectivity (FC) have become pivotal for understanding the large-scale network alterations associated with ASD. Despite ASD being a neurodevelopmental disorder, and FC being significantly influenced by the brain state, existing FC studies in mouse models predominantly focus on adult subjects under anesthesia. The differential impact of anesthesia and age on cortical functional networks in ASD subjects remains unexplored. To fill this gap, we conducted a longitudinal evaluation of FC across three brain states and three ages in the Shank3b mouse model of autism. We utilized wide-field calcium imaging to monitor cortical activity in Shank3b^{+/-} and Shank3b^{+/+} mice from late development (P45) through adulthood (P90), and isoflurane anesthesia to manipulate the brain state. Our findings reveal that network hyperconnectivity, emerging from the barrel-field cortices during the juvenile stage, progressively expands to encompass the entire dorsal cortex in adult Shank3b^{+/-} mice. Notably, the severity of FC imbalance is highly dependent on the brain state: global network alterations are more pronounced in the awake state and are strongly reduced under anesthesia. These results underscore the crucial role of anesthesia in detecting autism-related FC alterations and identify a significant network of early cortical dysfunction associated with autism. This network represents a potential target for non-invasive translational treatments.

Translational Psychiatry (2025)15:154; <https://doi.org/10.1038/s41398-025-03377-5>

INTRODUCTION

Autism spectrum disorders (ASDs) are a group of neurodevelopmental conditions characterized by deficits in social communication, interaction, and repetitive behaviors. Emerging evidence suggests that brain network dysfunction is central to the neurobiological basis of ASDs. Thus, functional connectivity (FC) studies are pivotal for exploring the interactions between brain regions and elucidating autism-related large-scale network dynamics.

Research has identified a range of hyper- and hypo-connected networks as primary alteration in adult mouse models of autism [1–4]. However, behavioral deficits and brain circuits anomalies are already evident from earlier postnatal stages [5]. While functional imaging during developmental stages has shown predictive value for autism diagnosis in humans [6], similar longitudinal studies in mice are lacking, particularly those that track FC from development through adulthood [5].

Furthermore, FC is influenced by brain state [7, 8] which in turn is frequently constrained by the imaging method used [9]. Functional Magnetic Resonance Imaging (fMRI) is the preferred technique for FC studies in mice due to its strong translational potential to humans. However, fMRI is typically conducted under anesthesia to prevent motion artifacts [10, 11]. Anesthesia can

preserve some functional networks while suppressing or altering others [9], making it challenging to validate FC results across different brain states. Although recent advances have enabled fMRI in awake head-fixed autistic mice [12, 13], mesoscale Ca²⁺ imaging offers a valuable alternative for investigating the cortical network across different brain states within the same subjects [14, 15]. Despite its limitations to near-surface recordings [16], this technique combines wide-field fluorescent microscopy (WFFM) with genetically encoded calcium indicators to directly measure neuronal activity [17, 18].

WFFM has recently been used to explore altered FC patterns during voluntary movements in the Shank3 mouse model of autism [4]. Shank3 is a postsynaptic scaffolding protein of excitatory synapses, whose reduced expression leads to impaired synaptic transmission and plasticity [5, 19]. It is known to cause Phelan-McDermid syndrome (PMS) and idiopathic autism [20–22]. Adult Shank3b mutant mice exhibit anxiety-like behavior, excessive self-injurious grooming, and altered whisker-dependent discrimination [1, 23, 24], suggesting significant cognitive and sensory dysfunctions.

In this study, we investigated the brain state-dependence of cortical network dynamics using mesoscopic Ca²⁺ imaging of

¹Neuroscience Institute, National Research Council, Pisa, Italy. ²European Laboratory for Non-Linear Spectroscopy, Sesto Fiorentino, Italy. ³Physics and Astronomy Department, University of Florence, Sesto Fiorentino, Italy. ⁴Interdisciplinary Health Science Center, Scuola Superiore Sant'Anna, Pisa, Italy. ⁵Department of Neurosciences, Psychology, Drug Research and Child Health (NEUROFARBA), University of Florence, Florence, Italy. ⁶Department of Health Sciences (DSS), University of Florence, Florence, Italy. ⁷Department of Developmental Neuroscience, IRCCS Stella Maris Foundation, Pisa, Italy. ⁸National Institute of Optics, National Research Council, Sesto Fiorentino, Italy.

email: montagni@lens.unifi.it; allegra@lens.unifi.it

Received: 28 August 2024 Revised: 19 March 2025 Accepted: 7 April 2025

Published online: 19 April 2025

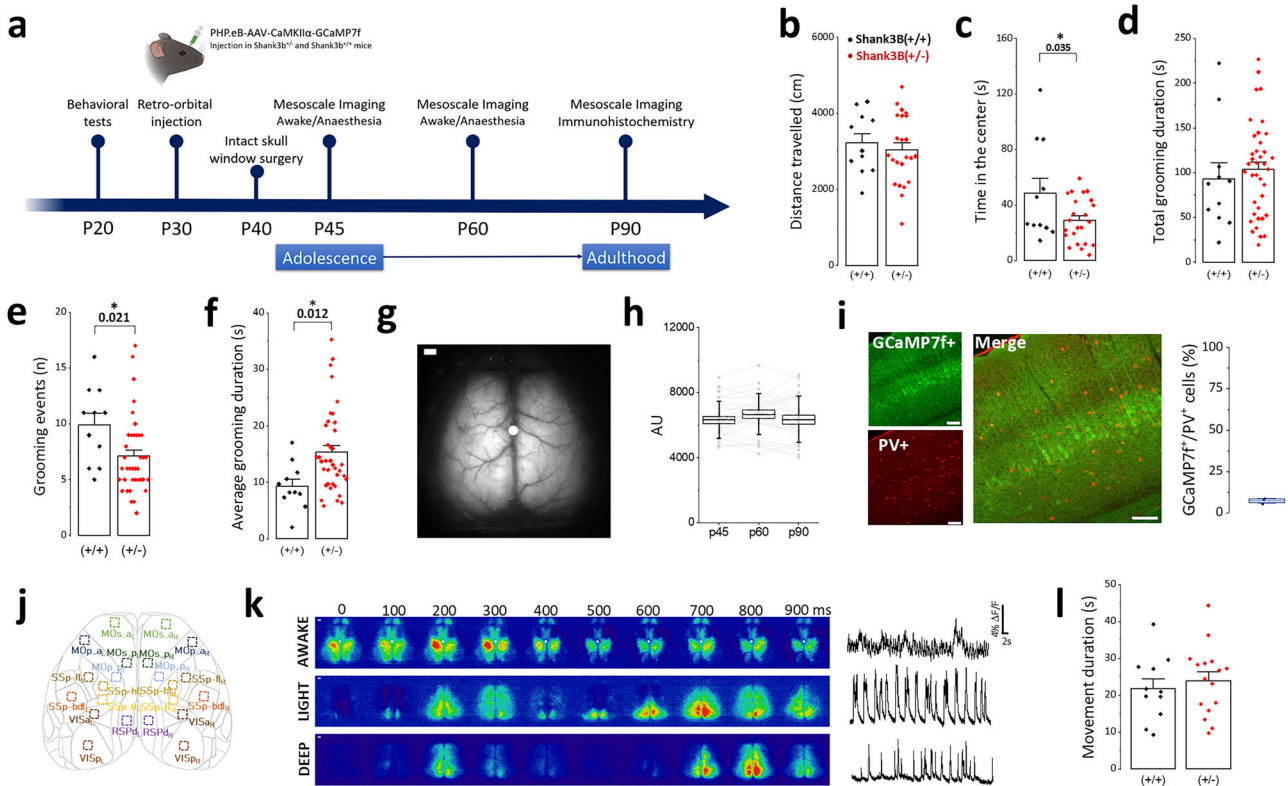


Fig. 1 Experimental design for cortical mesoscopic calcium imaging, immunohistochemical analysis and behavioral characterization of *Shank3b*^{+/-} mice. **a** Experimental timeline, with behavioral test at P20 followed by retro-orbital injection of AAV-PHP.eB GCaMP7f at P30, optical window implantation at P40 and longitudinal imaging timepoints at P45, P60 and P90. At the end of in vivo experiments, immunohistochemical analysis was performed. **b–f** Quantification of open field performance of *Shank3b*^{+/+} and *Shank3b*^{+/-} mice, **b** Total distance travelled (3220 ± 240 cm $n = 11$ *Shank3b*^{+/+}; 3034 ± 188 cm $n = 23$ *Shank3b*^{+/-}, two-sample t-test), **c** Time spent in the center of the arena (48 ± 10 s $n = 11$ *Shank3b*^{+/+}, 29 ± 3 s $n = 23$ *Shank3b*^{+/-}, $*p < 0.05$, two-sample t-test), **d** quantification of the total amount of self-grooming grooming (93 ± 18 s $n = 11$ *Shank3b*^{+/+}, 103 ± 8 s $n = 38$ *Shank3b*^{+/-}, two-sample t-test), **e** quantification of the number of self-grooming events (n) performed (9.9 ± 1.0 $n = 11$ *Shank3b*^{+/+}, 7.1 ± 0.5 $n = 38$ *Shank3b*^{+/-}, $*p < 0.05$, two-sample t-test). **f** Averaged duration of a single self-grooming event (9 ± 1 s $n = 11$ *Shank3b*^{+/+}, 15 ± 1 s $n = 38$ *Shank3b*^{+/-}, $*p < 0.05$, two-sample t-test). **g** Representative image of the field of view. White dots represent bregma, scalebar: 1 mm. **h** In vivo quantification of GCaMP7f expression across timepoints (6326 ± 223 AU - P45, 6679 ± 245 AU - P60, 6354 ± 277 AU - P90, $n = 27$, one-way repeated measure ANOVA). **i** Left, representative immunohistochemistry images showing the neuronal expression of GCaMP7f (green) and PV (red) in the whole cortical layers, scalebar: 100 μ m. Right, Quantification of the colocalization ratio GCaMP7f⁺/PV⁺ ($7.4 \pm 1.0\%$, $n = 3$ mice). **j** Cortical parcellation map with 10×10 ROI based on Allen Mouse Brain Atlas (see Methods). **k** Left, representative image sequences showing cortical activity in three different brain states (awake, light anesthesia and deep anesthesia). White dots represent bregma, scale bar: 1 mm. Right, representative single-trial time series showing averaged cortical activity in the same brain states. **l** Quantification of forepaw movement during imaging session at P45. *Shank3b*^{+/+} (black) and *Shank3b*^{+/-} (red) mice spent the same time doing movement (21.8 ± 2.6 s, $n = 11$ *Shank3b*^{+/+}; 23.9 ± 2.3 s, $n = 16$ *Shank3b*^{+/-}, two-sample t-test). Data represents mean \pm SEM, each dot represents one animal.

excitatory neurons expressing GCaMP7f in *Shank3b*^{+/+} and *Shank3b*^{+/-} mice. We longitudinally assessed cortical network alterations at three developmental stages, beginning at postnatal day 45 (P45) and extending to adulthood (P90). Our findings indicate that hyper-connectivity in the barrel cortices contributes significantly to the emergence of aberrant FC networks from juvenile stages, and a progressive strengthening and expansion of this overconnected network with age. Importantly, these network dysfunctions are not sustained under deep anesthesia. These results reveal a critical network of cortical dysfunction associated with autism, which may serve as a target for noninvasive translational therapies.

RESULTS

In this study, we first examined behavioral alterations in *Shank3b*^{+/-} mice at a juvenile stage (P20). We then assessed FC impairments at multiple developmental stages, from late adolescence (P45) to adulthood (P90), using WFFM. To understand how

cortical network alterations were influenced by brain state, we compared FC across different conditions: wakefulness, light anesthesia, and deep anesthesia. This approach allowed us to evaluate the impact of varying brain states on the altered cortical network.

Adolescent *Shank3b*^{+/-} mice exhibit anxiety and altered grooming behavior

Behavioral assessments of *Shank3b* mutant mice at various ages starting from late postnatal development (P45 to 6 months) have previously identified cognitive dysfunctions [1, 24]. To confirm behavioral anomalies present in our mouse mutant model, we investigated *Shank3b*^{+/-} mice at postnatal day 20 (P20, Fig. 1a). Generalized anxiety and locomotor activity were evaluated by using an open field arena. Although *Shank3b*^{+/-} mice traveled similar distances compared to their *Shank3b*^{+/+} littermates (Fig. 1b), they spent less time in the center of the arena (Fig. 1c), indicating heightened anxiety-like behavior without observable motor deficits. In line with previous study [24, 25], the

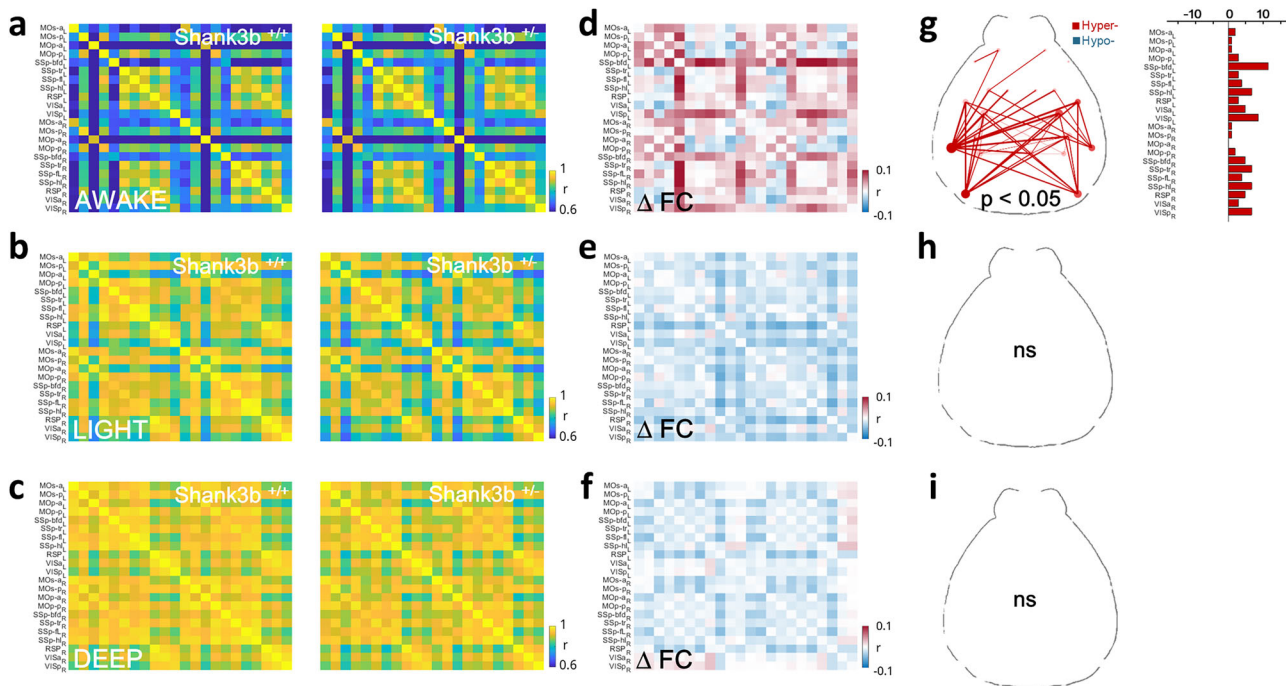


Fig. 2 Awake state hyperconnectivity of barrel field and visual cortices in adolescent *Shank3b*^{+/-} mice (P45). **a–c** Pairwise Pearson's correlation coefficients of cortical activity in a 3 min window were visualized as averaged correlation matrices for genotype (*Shank3b*^{+/+} left, *Shank3b*^{+/-} right) in the awake state (**a**), light anesthesia (**b**) and deep anesthesia (**c**). **d–f** Matrix of difference, produced by subtracting the average FC of *Shank3b*^{+/+} from that of *Shank3b*^{+/-} mice in the awake state **d**, light anesthesia (**e**) and deep anesthesia (**f**). Red and blue squares indicate *Shank3b*^{+/-} hyper- or hypo-connectivity respectively. **g–i** Network diagrams (left) of statistically significant FC alterations in the awake state (**g**), light anesthesia (**h**) and deep anesthesia (**i**). The bar plot (right) indicates the number of significant FC alterations for each cortical area. (*n* = 11 *Shank3b*^{+/+} and 17 *Shank3b*^{+/-}). Statistical test: NBS, *p* < 0.05.

total grooming time did not significantly differ between genotypes (Fig. 1d). However, *Shank3b*^{+/-} showed a reduced frequency of grooming episodes (Fig. 1e) and a notable tendency to engage in longer grooming bouts (Fig. 1f). These findings suggest that while overall grooming activity remains unchanged, *Shank3b*^{+/-} mice exhibit difficulties in interrupting repetitive behaviors, highlighting a specific grooming dysfunction.

AAV-PHP.eB delivered at postnatal day 30 induces long-term stable transgene expression in the cortex

To investigate the cortical patterns underlying functional impairments observed in adolescent *Shank3b*^{+/-} mice, we employed retro-orbital (RO) injections of a recently developed viral vector that effectively crosses the blood-brain barrier (BBB) [26, 27]. The viral vector, AAV-PHP.eB-CaMKII α -GCaMP7f, enables widespread transduction of the calcium indicator throughout the cortex (Supplementary Fig. 1), allowing for comprehensive detection of excitatory neuronal activity across the dorsal cortical mantle (Fig. 1g). We assessed the long-term stability of GCaMP7f expression by injecting AAV-PHP.eB-CaMKII α -GCaMP7f at P30 and measuring spatial fluorescence intensity profiles at three time points, i.e., P45, P60 and P90. GCaMP7f expression remained stable through P90 (Fig. 1h). To verify the specificity of CaMKII α promoter for excitatory neurons, we used an antibody against parvalbumin (PV) assessing the density of PV interneurons in post-mortem brain sections from P90 mice (Fig. 1i). Our results confirmed that the majority of PV-interneurons were not transfected, validating the promoter selectivity for targeting excitatory neurons (Fig. 1i).

This approach allowed us to capture cortical activity from 22 regions of interest (ROIs) across the entire dorsal cortex (Fig. 1j) during different brain states: wakefulness, light anesthesia and deep anesthesia (Fig. 1k). During the awake state, mice were head-restrained and free to move their limbs without specific tasks. The

average time spent in movement episodes during a 3 min awake imaging session was comparable between *Shank3b*^{+/-} and *Shank3b*^{+/+} mice (Fig. 1l). Anesthesia was modulated by adjusting isoflurane concentration between 1.3–1.7% in accordance with previous studies [14]. Light anesthesia resulted in longer Up-state durations (Supplementary Fig. 2b–d) and shorter Down-state durations (Supplementary Fig. 2a–c) compared to deep anesthesia in both genotypes. Up- and Down-state durations remained consistent across different time points (Supplementary Fig. 2). These data demonstrate that systemic administration of AAV-PHP.eB effectively induces selective and long-term stable expression of calcium indicator at the cortical level, enabling longitudinal mesoscale Ca²⁺ imaging in vivo in a mouse model of autism.

Awake state hyperconnectivity of barrel field and visual cortices in adolescent *Shank3b*^{+/-} mice

We first applied our approach to investigate cortical FC alterations in P45 *Shank3b*^{+/-} mice and their dependency on brain state. By characterizing FC at P45, we aimed to determine if early FC of excitatory neurons exhibited region-specific changes in *Shank3b*^{+/-} mice compared to their non-mutant littermates, and whether these abnormalities were preserved across different brain states. FC matrices were obtained by calculating Pearson's correlation coefficient (Fisher's z-transformed) between time traces of paired cortical regions after hemodynamic correction (Fig. 2a–c). We then computed differences between *Shank3b*^{+/+} and *Shank3b*^{+/-} mice within each brain state, obtaining a matrix of differences (Fig. 2d–f), and tested for significant changes in correlations using Network-Based Statistic (NBS, Fig. 2g) [4].

Consistent with previous studies [15], resting-state (rsFC) increased with higher levels of anesthesia (Fig. 2a–c). Although both genotypes exhibited this trend, genotype-specific effects were observed. Robust and symmetric hyperconnectivity was

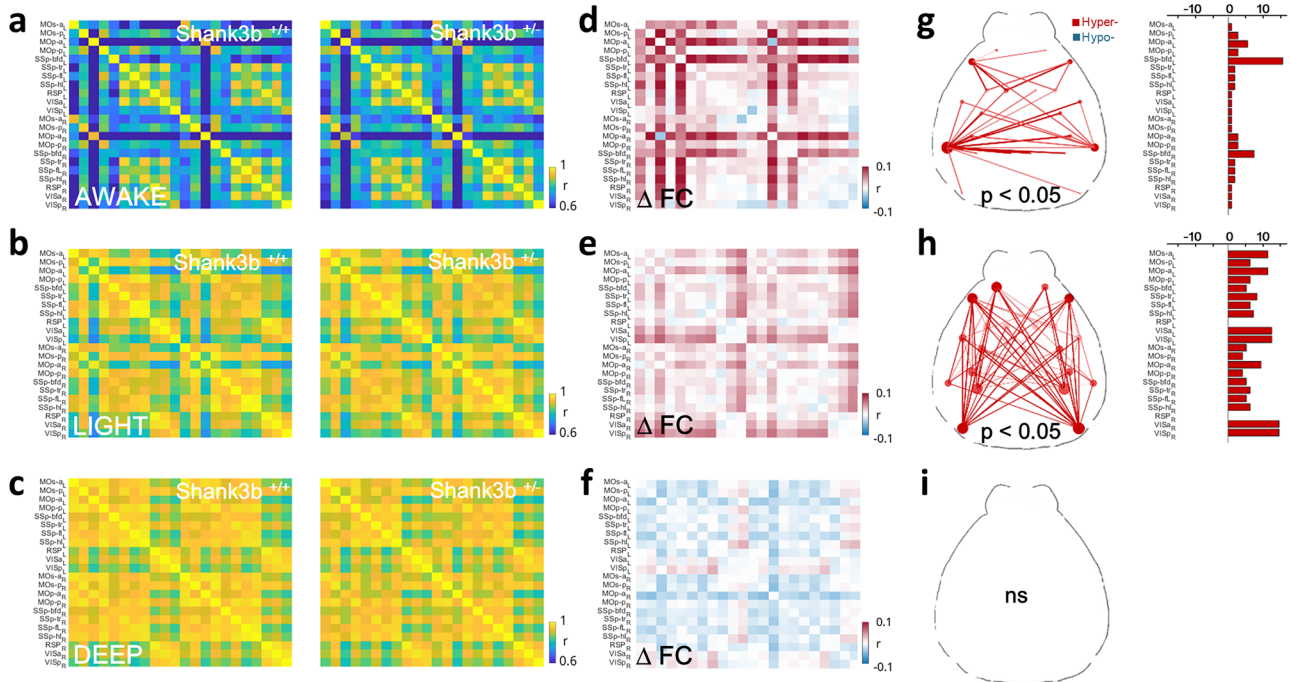


Fig. 3 Hyperconnectivity becomes more prominent and spreads to motor regions at P60. **a–c** Pairwise Pearson's correlation coefficients of cortical activity in a 3 min window were visualized as averaged correlation matrices for genotype (*Shank3b^{+/+}* left, *Shank3b^{+/-}* right) in the awake state **a**, light anesthesia (**b**) and deep anesthesia (**c**). **d–f** Matrix of difference, produced by subtracting the average FC of *Shank3b^{+/-}* from that of *Shank3b^{+/+}* mice in the awake state **d**, light anesthesia (**e**) and deep anesthesia (**f**). Red and blue squares indicate *Shank3b^{+/-}* hyper- or hypo-connectivity respectively. **g–i** Network diagrams (left) of statistically significant FC alterations in the awake state (**g**), light anesthesia (**h**) and deep anesthesia (**i**). The bar plot (right) indicates the number of significant FC alterations for each cortical area. ($n = 13$ *Shank3b^{+/+}* and 17 *Shank3b^{+/-}*). Statistical test: NBS. $p < 0.05$.

evident in the awake state of *Shank3b^{+/-}* mice compared to *Shank3b^{+/+}* mice (Fig. 2d). This hyper-connected network primarily involved the barrel field (SSp-bfd) and visual cortices (VISp, Fig. 2g), suggesting that the altered sensitivity to peripheral stimuli observed in *Shank3b* mutant mice [1] may arise from early network impairment. Under light (Fig. 2e) and deep anesthesia (Fig. 2f) *Shank3b^{+/-}* FC was instead similar to control mice, showing a non-significant trend toward global hypo-connectivity (Fig. 2h, i).

The substantial dependence of FC alterations on the brain state is indicated by the formation of a hyper-connected network in the waking state of *Shank3b^{+/-}* mice, which fades under anesthesia. These results underscore how crucial is to monitor the brain state when comparing FC between mutant mice and their wild-type littermates.

Hyperconnectivity becomes more prominent and spreads to motor regions at P60

To evaluate how the cortical network evolves with age, mice were monitored at P60. Interestingly, the hyper-connected network involving the SSp-bfd strengthened in the awake state of *Shank3b^{+/-}* mice at P60 (Fig. 3d, g). At this stage there was also an emergence of impairment in the anterior primary motor cortices (MOP-a) in *Shank3b^{+/-}* mice (Fig. 3g). In contrast to the results observed at P45, hyperconnectivity also emerged under light anesthesia at P60 (Fig. 3e). These significant alterations affected the entire cortical network, except for the retrosplenial cortices (RSP, Fig. 3h). Under deep anesthesia, there was a widespread but mild reduction in FC, with no significant alterations (Fig. 3f, i). Collectively, these results highlight the persistence and strengthening of a densely hyper-correlated subnetwork involving the barrel field cortex of both hemispheres over time in the awake state. Additionally, the spread of

hyperconnectivity to motor regions at P60 indicates a progression of network dysfunction as the mice age.

Alterations in functional connectivity persist at P90

To evaluate the persistence of altered FC from adolescence to adulthood, we examined cortical network activity at P90. A dense and widespread hyper-correlated cortical network emerged in the awake state (Fig. 4d, g), indicating that genotype-dependent differences in FC increased over time. Hyperconnectivity also persisted in lightly anesthetized P90 mice (Fig. 4e, h). However, under deep anesthesia, *Shank3b^{+/-}* mice exhibited a non-significant trend towards hypo-connectivity compared to *Shank3b^{+/+}* mice (Fig. 4f, i). Taken together, these results suggest a robust dependence of the altered network on the brain state, enduring from P45 to P90. The progression of hyperconnectivity in awake and lightly anesthetized states underscores the persistent and evolving nature of network dysfunction in *Shank3b^{+/-}* mice.

Network alterations are strongest in the awake state

Given that FC alterations intensified and spread across the entire cortex between P45 and P90 in both the awake state and under light anesthesia, we compared the temporal evolution of the average global FC between genotypes in each brain state separately.

Interestingly, *Shank3b^{+/+}* global FC remained stable over time in all three brain states investigated (Fig. 5). In contrast, *Shank3b^{+/-}* global FC significantly increased from P45 to P90 in both the awake state and under light anesthesia (Fig. 5a, b). Under deep anesthesia, global FC trends in *Shank3b^{+/-}* were similar to those in *Shank3b^{+/+}* mice, with no significant differences (Fig. 5c). It is important to note that FC changes under anesthesia are not influenced by the brain state, as the Up- and Down-state durations were consistent across

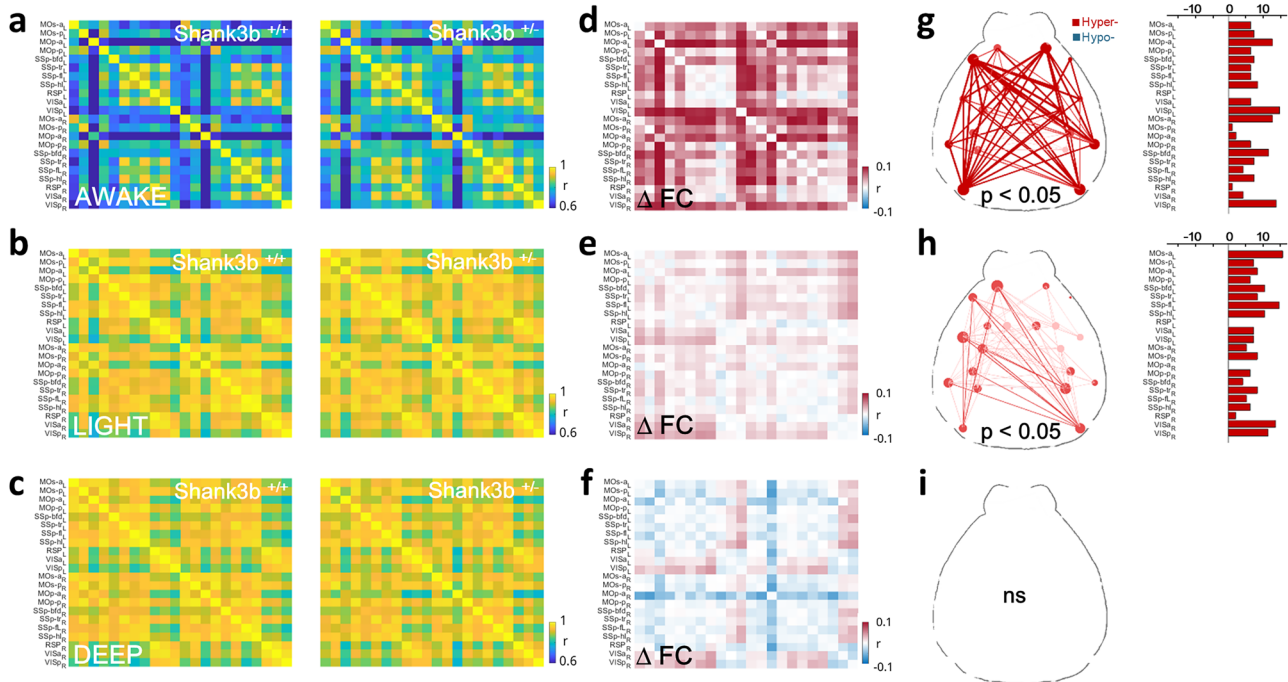


Fig. 4 Alterations in functional connectivity persist at P90. **a–c** Pairwise Pearson's correlation coefficients of cortical activity in a 3 min window were visualized as averaged correlation matrices for genotype ($Shank3b^{+/+}$ left, $Shank3b^{+/-}$ right) in the awake state (**a**), light anesthesia (**b**) and deep anesthesia (**c**). **d–f** Matrix of difference, produced by subtracting the average FC of $Shank3b^{+/+}$ from that of $Shank3b^{+/-}$ mice in the awake state (**d**), light anesthesia (**e**) and deep anesthesia (**f**). Red and blue squares indicate $Shank3b^{+/-}$ hyper- or hypo-connectivity respectively. **g–i** Network diagrams (left) of statistically significant FC alterations in the awake state (**g**), light anesthesia (**h**) and deep anesthesia (**i**). The bar plot (right) indicates the number of significant FC alterations for each cortical area. ($n = 13$ $Shank3b^{+/+}$ and 14 $Shank3b^{+/-}$). Statistical test: NBS. $p < 0.05$.

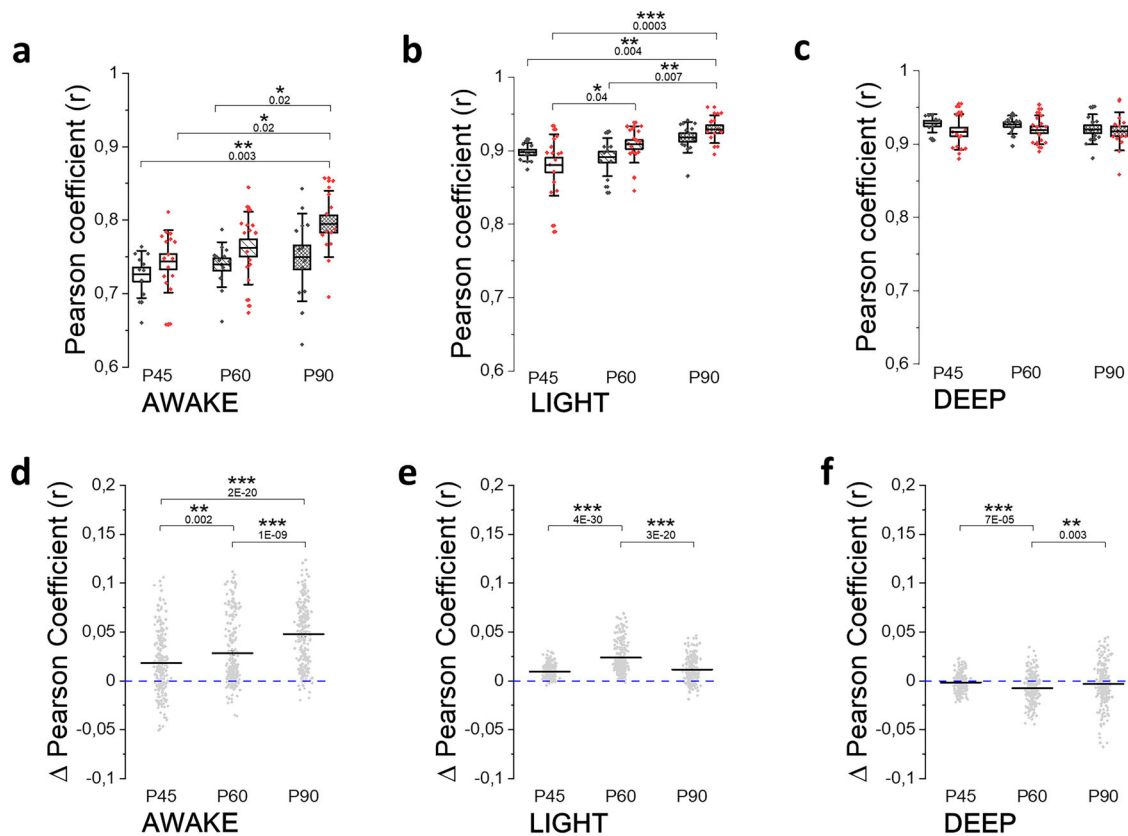


Fig. 5 Network alterations are stronger in the awake state and increase over time. **a–c** Box plots of global functional connectivity across time for both the genotypes ($Shank3b^{+/+}$ black, $Shank3b^{+/-}$ red) in the awake state (**a**) light anesthesia (**b**) and deep anesthesia (**c**) ($*p < 0.05$; $**p < 0.01$; $***p < 0.001$, two-way ANOVA). **d–f** Longitudinal monitoring of difference in Pearson coefficient between $Shank3b^{+/-}$ and $Shank3b^{-/-}$ in awake (**d**), light (**e**) and deep anesthesia (**f**). $*p < 0.05$; $**p < 0.01$; $***p < 0.001$, one-way ANOVA.

time and genotypes (Supplementary Fig. 2a, b). Further analysis revealed that FC alterations between $\text{Shank3b}^{+/+}$ and $\text{Shank3b}^{+/-}$ were more pronounced in the awake state and intensified over time (Fig. 5d–f). This demonstrates a robust hyper-connectivity of the cortical network in awake $\text{Shank3b}^{+/-}$ mice starting from a juvenile age. Moreover, these results highlighted that the severity of connectivity imbalance is highly dependent on the brain state: network alterations are more pronounced in the awake state and tend towards hypoconnectivity under anesthesia (Fig. 5d–f).

FC changes in $\text{Shank3b}^{+/-}$ mice are preserved after global signal regression analysis

Previous studies have demonstrated that removing the mean signal with Global Signal Regression (GSR) analysis can reveal network alterations that might be hidden by global activity patterns [28–30]. To this aim, we applied GSR to our calcium imaging data. After GSR pre-processing, distinct networks of altered FC emerged across different brain states and developmental time points. Notably, the significant alterations observed under light anesthesia at all time points were no longer present and the early differences detected in the awake state at P45 disappeared (Supplementary Fig. 3). At P60, in the awake state, an alternating pattern emerged, with hyperconnectivity in the motor cortices and barrel field, while the retrosplenial cortex (RSP) exhibited hypoconnectivity (Supplementary Fig. 4). At P90, the most striking finding was the reversal in the sign of genotype-related FC difference between the awake state and deep anesthesia: the RSP, hypoconnected in the awake state, displayed hyperconnectivity under deep anesthesia in $\text{Shank3b}^{+/-}$ compared to $\text{Shank3b}^{+/+}$ mice. In contrast, motor and barrel field cortices exhibited hypoconnectivity in deep anesthesia (Supplementary Fig. 5), consistent with findings from previous studies using other imaging techniques [31]. These results indicate that specific cortical regions in the same neural circuit can show opposite patterns of dysregulation depending on the brain state.

Moreover, we confirm that FC alterations in $\text{Shank3b}^{+/-}$ mice become more pronounced with increasing age, with the network exhibiting increasingly greater deviations from $\text{Shank3b}^{+/+}$ mice by P90 across all brain states (awake, light and deep anesthesia). This result suggests a progressive dysregulation of network dynamics regardless of the pre-processing analysis, reinforcing the notion that ASD-related connectivity impairments worsen with age.

Elevated response to spontaneous excitatory inputs in the SSp-bfd of adult $\text{Shank3b}^{+/-}$ mice

Given the persistent alterations in large-scale excitatory FC of the barrelfield cortex from the early time point investigated, and considering that this region has already been identified as altered in adult $\text{Shank3b}^{-/-}$ mouse models, we investigated the underlying synaptic dysfunctions in SSp-bfd neurons at P90. Whole-cell recordings were conducted on ex-vivo brain slices from $\text{Shank3b}^{+/+}$ and $\text{Shank3b}^{+/-}$ mice, specifically targeting layer V pyramidal neurons of the SSp-bfd. Firstly, we evaluated the basic electrophysiological properties and detected no changes in the membrane capacitance, membrane resistance and resting membrane potential (Fig. 6a).

We then examined the intrinsic excitability of layer V pyramidal neurons by measuring the action potential threshold and the number of action potentials evoked by depolarizing steps of increasing amplitude (Fig. 6d). As shown in Fig. 6b, c, we found no differences in these measures, suggesting that the mutation does not influence intrinsic excitability. As a proxy for single-cell and local connectivity, we recorded spontaneous excitatory postsynaptic currents (sEPSCs). This analysis revealed no effect of genotype on the frequency of sEPSCs, while the amplitude of sEPSCs was found elevated in $\text{Shank3b}^{+/-}$ compared to non-mutant littermates (Fig. 6f), indicating heightened sensitivity to

excitatory inputs in the SSp-bfd neurons, but in presence of unaltered local network excitation. To establish a link between in vivo FC and microscale activity in brain slices, each electrophysiological parameter was used to perform a cross-correlation analysis with SSp-bfd FC (Supplementary Fig. 6). A significant correlation was revealed between SSp-bfd FC and resting potential (Supplementary Fig. 6c) and between SSp-bfd FC and sEPSC frequency (Supplementary Fig. 6e) in $\text{Shank3b}^{+/+}$ animals. Interestingly, such correlations are lost in the $\text{Shank3b}^{+/-}$ group.

These findings provide a potential synaptic mechanism underlying the observed global hyperconnectivity in the cortical network of $\text{Shank3b}^{+/-}$ mice, emphasizing the role of enhanced synaptic strength in the altered FC associated with this model of autism.

DISCUSSION

This study aimed to address the gap in autism-related FC research, which predominantly focuses on adult stages. Autism is a neurodevelopmental disorder, yet there is a scarcity of studies examining brain connectivity during development in rodent models. Additionally, how brain states differentially affect cortical functional networks in autistic subjects remains largely unexplored.

Since SHANK3 haploinsufficiency has been associated with neurobehavioral abnormalities in individuals with Phelan-McDermid Syndrome (PMS), we focused on Shank3 heterozygous mice generated by crossing wild-type mice with heterozygotes to be most relevant to the clinical syndrome. Previous research has mainly focused on Shank3b knockout mice ($\text{Shank3b}^{-/-}$) due to their more pronounced behavioral defects. However, heterozygous SHANK3 mutations or loss are considered a major cause of PMS in humans [20]. Thus, $\text{Shank3b}^{+/-}$ mice offer a more relevant model for studying cortical FC alterations.

We used mesoscale cortical imaging to study excitatory neuron activity in $\text{Shank3b}^{+/-}$ mice, tracking changes from late adolescence to adulthood. We utilized retro-orbital injection of AAV-PHP.eB-GCaMP7f at P30, achieving effective and stable transduction of excitatory neurons across the dorsal cortex with a strong tropism for layer V (L5) pyramidal neurons. This method provides a reliable tool for monitoring cortical activity across ages [32, 33] and avoids the high costs and time associated with crossbreeding genetically modified mice with GECI-expressing strains [34].

Behavioral assessments revealed generalized anxiety and repetitive behaviors in young $\text{Shank3b}^{+/-}$ mice (P20), consistent with previous findings of neophobia and over-grooming in $\text{Shank3b}^{+/-}$ mice at later stages [23, 24, 35]. Moreover, we found that early alterations in the cortical somatosensory network were evident by P45, persisting until adulthood (P90). These results support the hypothesis that somatosensory connections are already well-established before adolescence (P15) [36] and that an early excitation/inhibition (E/I) imbalance and myelin defects during the early stage of development - before P21 - may be an essential mechanism leading to alterations in behavior and FC [37–39].

Altered connectivity in the motor cortices emerged later (P60), likely reflecting late maturation processes [36]. Indeed, anterior portions of the brain, including prefrontal cortices, undergo late maturation: motor, visual and retrosplenial cortices connections significantly changed between P22 and P60 in healthy mice [36, 40]. These findings align with reports of hyper-connected cortical patterns involving motor areas in other autism mouse models during wakefulness [4].

The progressive alterations in FC from P45 to P90 may result from a gradual deterioration of circuit function with age, which is consistent with the high rate of regression reported in PMS patients. Neurodevelopmental regression is a key feature of PMS [41], with affected individuals showing a distinctive pattern of regression

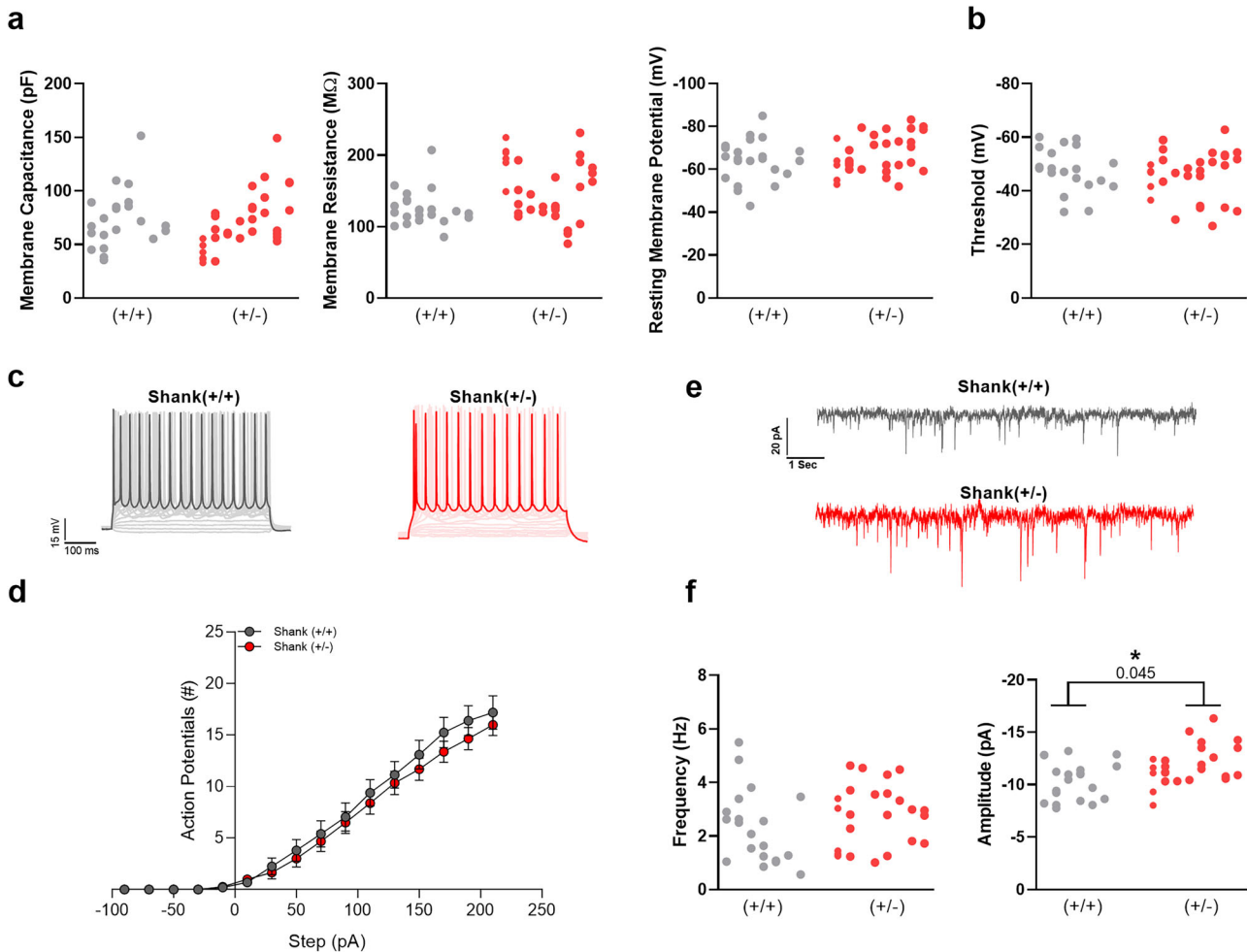


Fig. 6 Characterization of layer V pyramidal neurons of SSp-bfd. **a** Passive properties such as membrane capacitance (left, 74.28 ± 5.65 pF, $n = 7$ Shank3b^{+/+} mice, $N = 22$ cells; 70.53 ± 4.76 pF, $n = 8$ Shank3b^{+/-} mice, $N = 31$ cells), membrane resistance (middle, 125.6 ± 5.32 m Ω , $n = 7$ Shank3b^{+/+} mice, $N = 22$ cells; 152.3 ± 7.45 m Ω , $n = 8$ mice, $N = 31$ cells), and resting membrane potential (right, -64.2 ± 2.067 mV, $n = 7$ mice Shank3b^{+/+}, $N = 22$ cells; -67.06 ± 1.58 mV, $n = 8$ Shank3b^{+/-} mice, $N = 31$ cells) in Shank3b^{+/+} (black) and Shank3b^{+/-} mice (red). **b** Action potential threshold (-47.89 ± 1.67 mV, $n = 7$ Shank3b^{+/+} mice, $N = 21$ cells; -47.24 ± 1.57 mV, $n = 8$ Shank3b^{+/-} mice, $N = 31$ cells). **c** Representative current clamp traces obtained by 500 ms steps of increasing depolarizing current ranging from -90 to $+210$ in 20 pA increments. Bold traces show the action potential firing at 210 pA current input in Shank3b^{+/+} (grey) and Shank3b^{+/-} (red). **d** Current-AP curves obtained by plotting the mean number of AP evoked against current input amplitude ($n = 7$ Shank3b^{+/+} mice, $N = 20$ cells; $n = 8$ Shank3b^{+/-} mice, $N = 26$ cells). **e** Representative whole-cell recordings of sEPSCs from Shank3b^{+/+} (grey) and Shank3b^{+/-} (red) mice. **f** Bars graph of absolute (dots) and average (bars) measure of sEPSCs frequency (left, 2.32 ± 0.33 Hz, $n = 7$ Shank3b^{+/+} mice, $N = 18$ cells; 2.764 ± 0.24 Hz, $n = 8$ Shank3b^{+/-} mice, $N = 24$ cells) and amplitude (right, -10.32 ± 0.42 pA, $n = 7$ Shank3b^{+/+} mice, $N = 18$ cells; -11.88 ± 0.38 pA, $n = 8$ Shank3b^{+/-} mice, $N = 24$ cells) in both genotypes. Data are presented as mean \pm SEM, each dot represents one animal. *p*-values were obtained from the LMM, and significance was defined as **p* < 0.05.

through several stages across the lifespan. Notably, regression in PMS primarily affects motor and self-help skills [42], which corresponds with our findings that indicate a later involvement of motor cortices in FC alterations. However, it is important to note that rs-fMRI studies have shown hypo-connectivity within the somatosensory-hippocampal network and prefrontal regions in Shank3b^{+/-} mice under anesthesia [1, 31].

Consolidating our previous work on the brain state dependence of the FC in healthy subjects [14], this study demonstrates how brain states significantly impact network dynamics in autistic mice. Across all investigated time points, there is a discernible shift from hyper- to hypo-connectivity in Shank3b^{+/-} mice compared to Shank3b^{+/+} mice when transitioning from wakefulness to anesthesia. This finding reconciles the seemingly conflicting results from different studies, highlighting the crucial role of brain state in modulating cortical functional connectivity in this autism model.

Results obtained with GSR, further supports these findings, by revealing extended networks of FC alterations across brain states and ages. GSR is widely reported for resting-state fMRI [43] and has recently been applied in calcium imaging in healthy subjects [30]. GSR applications can improve the correspondence between functional and anatomical connectivity in humans and help eliminate non-neuronal sources of global variance such as respiration and movement-related artifacts [29]. In our study, the imaging system was designed to minimize artifacts related to head movements. Moreover, the stability of the brain state during anesthesia (Supplementary Fig. 2) reduced variability in heartbeat and respiration between genotypes. These factors suggest that the observed global signal differences could reflect meaningful alterations in large-scale network activity. Interestingly, the lack of significant FC differences after GSR in light anesthesia (Supplementary Figs. 3–5) indicates that ASD-related alterations in this brain state may largely result from global synchronization, a

predominant feature of brain activity under isoflurane anesthesia [44]. Although GSR is widely applied in FC analysis [29], there is ongoing debate regarding possible consequences on biologically meaningful correlations [45]. Consistently with previous findings [43], when GSR is not applied resting-state correlation distributions are heavily skewed towards positive values. However, in Autism Spectrum Disorder (ASD), GSR has been found to hinder the detection of meaningful relationships between connectivity and behavioral measures [46, 47]. Our results highlight the importance of comparing results with and without GSR for ensuring robust and biologically meaningful conclusions [43].

Patch clamp recordings in brain slices indicate that Shank3 haploinsufficiency does not lead to major alterations in basic membrane properties and intrinsic excitability of L5 pyramidal neurons of the SSp-bfd. In terms of local connectivity, the significant increase in the amplitude of excitatory synaptic currents in Shank3b^{+/-} mice suggests elevated sensitivity towards synaptic excitation, a finding consistent with increased SSp-bfd FC in this group. However, when we performed a same-animal, cross-correlation analysis of SSp-bfd FC versus each electrophysiological parameter, we failed to reveal a linear relationship between SSp-bfd FC and sEPSC amplitude, regardless of the genotype. In summary, these results suggest that hyperconnectivity observed in this genotype may not solely result from alterations of single cell excitability or local connectivity.

Based on these findings of abnormally higher connectivity in awake Shank3b^{+/-} mice, we speculate that the cortical network of the mutants does not reach full maturation, possibly due to developmental miswiring [48]. Previous studies have shown that the dynamic process of over-connectivity followed by pruning, which occurs at neuronal level, also operates at the systems level, fostering the reshaping and balancing of connectivity in the developing brain [49]. Accordingly, brain networks in children present lower levels of hierarchical organization and modularity [50]. In the incompletely mature brains of Shank3b^{+/-} mice, this could result in undifferentiated and synchronous activation of an overconnected functional network. Exogenous induction of synchronous activity with isoflurane anesthesia might dampen the FC difference between the two genotypes by increasing the FC in wild-type mice in a dose-dependent manner. This suggests that the FC abnormalities observed in awake Shank3b^{+/-} mice might be masked or mitigated under anesthesia, highlighting the importance of considering brain state in the analysis of cortical network dynamics in autism models.

In summary, our study provides valuable insights into the complexity of autism-related cortical connectivity alterations from late development to adulthood. Our findings highlight behavioral anomalies at an early age (P20), a hyper-connected network involving barrel-field cortices during late adolescence (P45), and progressive deterioration over time until P90. We also demonstrated that brain state strongly influences cortical network dynamics: alterations are more pronounced in the awake state compared to under anesthesia, with divergent directions observed. We have provided unbiased and quantitative biomarkers based on FC that hold high translational value for assessment, follow-up, and therapeutic development of PMS. These biomarkers will be fundamental for both preclinical and potentially clinical testing of novel therapeutic strategies.

Limitations of the study

In this study GCaMP activity of excitatory neurons was longitudinally recorded at cortical level starting at postnatal day 45 (P45). Although autism spectrum disorders are neurodevelopmental disorders, conducting longitudinal imaging on the same subject with a cranial window implanted at an early developmental stage (before P40) is challenging due to the changes in skull size that occur throughout development. Moreover, wide-field calcium signals reflect the aggregate activity from soma, dendrites and axons within the

transfected cortical volume. As a result, our ability to pinpoint the signal's origin within specific cortical layers is limited.

METHODS

Ethical statement

A total of 78 B6.129-Shank3^{tm2Gfng/J} (3–12 weeks old) of both sexes were used. The Shank3b- knockout allele has a neo cassette replacing the PDZ domain (exons 13–16) of the Shank3 gene. The calculation of the sample size was performed using the G*power Software, comparing Shank3 mutant animals and their non-mutant littermates, both males and females, at different time points (p45, p60, and p90), for a total of 2 different experimental groups. An ANOVA test (repeated measures, within-between interactions) was applied, considering an effect size $f = 0.2$; α error probability = 0.05; power = 0.8; Number of groups = 2; Number of measures = 3. The resulting sample size was 26. In this study, Shank3b^{+/-} ($n = 17$) and Shank3b^{+/+} control littermates ($n = 13$) were used for mesoscopic calcium imaging (6–12 weeks old). Shank3b^{+/-} ($n = 38$) and Shank3b^{+/+} control littermates ($n = 11$) were used for behavioral experiments (3 weeks old). All animals were housed in standard condition cages with a 12 h light/dark cycle and food and water ad libitum. All experiment procedures were performed in accordance with the relevant guidelines and regulation and were approved by the Italian Ministry of Health, Authorization n. 721/2020.

The animals used in each experiment were assigned to each group based on the genotype and the investigators were blinded to the group allocation during the experiments and behavioral analysis.

Virus injection and intact-skull window

For CaMKII labeling with GCaMP7f, the viral construct ssAAV-PHPH.eB/2-mCaMKII α -jGCaMP7f-WPRE-bGHp(A) (1.3x10E13 vg/ml, volume: 50 μ L, Viral Vector Facility, CH) were diluted in 100 μ L of saline solution. A final volume of 150 μ L was intravenously injected in the retroorbital sinus of Shank3b^{+/-} and Shank3b^{+/+} mice under isoflurane anesthesia at P30, two weeks before imaging. One week before imaging the same animals were anesthetized with isoflurane (3% for induction, 1–2% for maintenance) and placed in a stereotaxic apparatus (KOPF, model 1900). Ophthalmic gel (Lacrilube) was applied to prevent eye drying; body temperature was maintained at 36 °C using a heating pad and lidocaine 2% was used as local anesthetic. The skin and the periosteum were cleaned and removed, then bregma and lambda were signed with a black fine-tip pen. A custom-made aluminum head-fixing bar was placed behind lambda and the exposed skull was fixed using transparent dental cement (Super Bond C&B – Sun Medical). After the surgery, mice were recovered in a temperature- and humidity-controlled room, with food and water ad libitum.

Wide-field microscopy setup

Wide-field imaging was performed using a custom-made microscope, as in Montagni and colleagues [14]. The microscope consisted of back-to-back 50 mm f/1.2 camera lenses (Nikon). To excite the GCaMP7f indicator, a 470 nm light source (LED, M470L3, Thorlabs, New Jersey, United State) filtered by a bandpass filter (482/18 Semrock, Rochester, New York, NY, USA) was deflected by a dichroic mirror (DC FF 495-DI02 Semrock, Rochester, New York, NY, USA) on the objective (TL2X-SAP 2X Super Apochromatic Microscope Objective, 0.1NA, 56.3 mm WD, Thorlabs). Reflectance images were acquired using a light source positioned at 45° incident to the brain surface (530 nm LED light, M530L4; Thorlabs, New Jersey, United State). Stroboscopic illumination (20 Hz/LED) was used. The fluorescence and reflectance signals were selected by a bandpass filter (525/50 nm filter, Semrock, Rochester, New York, USA) and collected by a CMOS camera (ORCA-Flash4.0 V3 Digital CMOS camera / C13440-20CU, Hamamatsu). Images were acquired at 40 Hz, with a resolution of 512 × 512 pixels (FOV of 11.5 × 11.5 mm).

Habituation and awake imaging

After the post-surgical recovery period (3 days), mice were acclimatized to the head-fixation for two consecutive days (15 min a day/mouse) to gradually reduce anxiety and abrupt movements prior to data collection. 14 days after the injection, head-fixed imaging sessions were performed at different timepoints (P45, P60 and P90). Each imaging session consisted of 4 recordings (180 s-long) of spontaneous cortical activity in awake, resting-state mice that could freely move their limbs and weren't engaged in any distinct tasks.

Anesthetized imaging

The same mice that did the awake imaging were then anesthetized by isoflurane to investigate spontaneous cortical activity in two brain states classified according to the isoflurane concentrations in DEEP anesthesia ($1.8 \pm 0.1\%$) and LIGHT anesthesia ($1.1 \pm 0.1\%$). Each anesthesia level was maintained for 60 min, and recordings were consistently monitored to conserve a stable slow-oscillatory regime. Imaging sessions (180s-long, 5 repetitions) were performed at different timepoints (P45, P60 and P90). Deep and light anesthesia were recorded consecutively on the same imaging session per mouse, starting from the higher isoflurane concentration to the lower. During the whole anesthetic treatment, body temperature was maintained at 37°C by a feedback-controlled thermostatic heating pad.

Image processing and data analysis

All data analyses were performed in MATLAB (MathWorks), Python, ImageJ, and Origin.

Image stacks for each animal collected from different sessions were registered using custom-made software, by considering bregma and λ position. An animal-specific field of view (FOV) template was used to manually adjust the imaging field daily. To dissect the contribution of each cortical area, we registered the cortex to the surface of the Allen Institute Mouse Brain Atlas (www.brain-map.org) projected to our plane of imaging. For each block, image stacks were processed to obtain the estimates of $\Delta F/F_0$. $\Delta F/F_0$ was computed for each pixel, where ΔF was the intensity value of that pixel in a specific time point and F was the mean fluorescence intensity of the signal across time. Then, hemodynamic correction was performed as described by Scott and colleagues [51]. Briefly, using the ratiometric approach:

$$\frac{F}{F_0} = \frac{I^{482}}{I^{682}} \frac{I^{625}}{I^{525}}$$

Where F/F_0 is the final corrected GCaMP6 time series for a given pixel, I^{482} refers to the detected fluorescence signal, I^{525} is the reflectance signal. Subsequently, GSR was applied.

In this study we focus on the analysis of the functional cortical network between Shank3b^{+/-} and Shank3b^{+/+}. To analyze FC, a total of 22 ROIs were then selected (11 ROI for each hemisphere, 20x20 pixels). The abbreviations and extended names for each areas are as follows: MOs-a, anterior region of secondary motor cortex; MOs-p, posterior region of secondary motor cortex; MOP-a, anterior region of primary motor cortex; MOP-p, posterior region of primary motor cortex; SSp-bfd, primary somatosensory area, barrefield; SSp-tr, primary somatosensory area, trunk; SSp-fL, primary somatosensory area, forelimb; SSp-hL, primary somatosensory area, hindlimb; RSP, retrosplenial cortex; VISa, associative visual cortex; VISp, primary visual cortex. Throughout the text and figures, suffixes L and R were added to denote cortical areas of the left or right hemisphere, respectively (e.g., RSP_L, RSP_R). Correlation mapping was done for each subject by computing Pearson's correlation coefficient between the average signals extracted from a ROI, with that of each other ROIs (time window: 180 s-long) and then averaged within a session. The averaged single-subject correlation maps were transformed using Fisher's r-to-z transform and averaged across all animals within a group. Then, the group-related averaged maps previously obtained were re-transformed to correlation values (r-scores).

Differences between groups were calculated as $r(\text{Shank3b}^{+/-}) - r(\text{Shank3b}^{+/+})$ of the averaged correlation values, to visualize matrices of difference at all the time points. ROIs positions in FC graphs were arranged according to their anatomical coordinates. Lines and symbol sizes represented the level of correlated FC and the number of such connections associated with the ROI, respectively.

Two animals were excluded from both imaging analysis at P90 and the consequent ex-vivo analysis due to an infection that compromised the field of view (FOV).

Behavioral analysis

Open field. Open field test was conducted on postnatal day 20 (P20). Prior to the trial, mice were habituated to the experimental room for 2 h. Then, mice were allowed to freely explore an empty arena ($45 \times 45 \times 45$ cm) for 10 min. The arena walls were white colored and smooth. Before the animal placement, the arena was washed with a 70% alcohol/water solution avoiding possible biasing effects from odor cues. The session was recorded with a camera (PointGrey flir Chameleon3, CM3-U3-13Y3C-CS), frame rate

was 30 fps. An experienced observer quantified the time spent self-grooming, which included behaviors such as cleaning the face, snout with paws, licking or biting the body. Videos were also automatically analyzed by Animal Tracker tool (ImageJ) to measure distance traveled and time spent in the center.

Movements during imaging session. At P45, to quantify movements during the imaging session, a camera (PointGrey flir Chameleon3, CM3-U3-13Y3C-CS) was orthogonally placed 10 cm in front of the mouse. The camera operated at a frame rate of 40 Hz, capturing images at a resolution of 512 by 512 pixels. This resolution provided sufficient detail to cover the frontal part of the mouse, allowing comprehensive analysis of movements. To well identify movements, visible illumination light at 630 nm was focused on the forepaws. Videos were then analyzed by an experienced observer to quantify time doing forepaw movements, including tapping and grooming.

Brain slices preparation and electrophysiology recordings

Adult (p90) Shank3 mice were deeply anesthetized with isoflurane and decapitated for brain extraction. Acute coronal slices ($350 \mu\text{m}$ thick) containing the primary somatosensory cortex (SSp-bfd) were cut with a vibraslicer (Leica VT1000S, Leica Microsystem, Wetzlar, Germany) in ice-cold carboxygenated cutting solution containing in (mM): Sucrose (206), Glucose (25), NaHCO₃ (25), KCl (2.5), NaH₂PO₄ (1.25), MgSO₄ (3), CaCl₂ (1). Slices recovered for a minimum of 1 h in warm ($32\text{--}34^\circ\text{C}$), carbon-oxygenated, low-calcium artificial cerebrospinal fluid (aCSF) with the following concentrations (mM): NaCl (130), KCl (3.5), NaH₂PO₄ (1.25), NaHCO₃ (25), Glucose (10), CaCl₂ (1) and MgSO₄ (2). Slices were individually transferred to a recording chamber placed under the objective of an upright microscope (Nikon Eclipse E600FN). During recordings, slices were continuously perfused with warm ($32\text{--}34^\circ\text{C}$) carbo-oxygenated, high-calcium aCSF solution composed of (in mM): NaCl (130), KCl (3.5), NaH₂PO₄ (1.25), NaHCO₃ (25), glucose (10), CaCl₂ (2) and MgSO₄ (4). Whole-cell electrophysiological recordings were performed with borosilicate capillaries (Harvard Apparatus, London, UK) made by a vertical puller (Narishige PP830, Narishige International Ltd, London, UK) and, back-filled with K⁺-gluconate-based internal solution contained (in mM): 120 K-Gluconate, 15 KCl, 10 HEPES, 1 EGTA, 2 MgCl₂, 5 Na₂Phosphocreatine, 0.3 Na₂GTP, and 4 MgATP (pH 7.3, 295–305 mOsm), resulting in a bath resistance of 3–4 M Ω . Layer V Pyramidal neurons of SSp-bfd were studied by recording passive properties (membrane capacitance, membrane resistance, and resting membrane potential), intrinsic excitability (Current-action potential curves and action potential threshold), and spontaneous excitatory post-synaptic currents (sEPSCs) isolated by the application of $10 \mu\text{M}$ SR95531 (GABAA receptor blocker). Current-Action potential curves were obtained with the injection of increasing steps (500 ms) of depolarizing current ranging from -90 to $+210$ pA increments. The threshold for action potential (AP) was determined at the base of the first spike. sEPSCs were recorded in voltage-clamp configuration holding the potential at -70 mV. All signals were sampled at 10 kHz and low-pass filtered at 2 kHz with an Axon Multiclamp 700B (Molecular Devices, Sunnyvale, CA, USA).

Ex-vivo imaging and histology

PV histological quantification and GCaMP expression in PHP.eB-injected mice were verified with post mortem histology at P90. Mice were transcardially perfused with 20 mL of 0.1 M phosphate-buffered saline (PBS, pH 7.6) and 100 mL of 4% paraformaldehyde (PFA). Coronal brain slices ($100 \mu\text{m}$ thickness) were cut using a vibratome (Vibratome Series 1500-Tissue Sectioning System).

For immunostaining, brain slices were incubated in a blocking solution for 1 h at room temperature (1% BSA; 0.1% Triton X-100 in PBS), washed 3 times with 0.1% Triton X-100 in PBSA and treated with primary antibody overnight at 4°C (Anti-PV, (1:500), abcam, ab11427). Following 3 washes in PBS, slices were incubated for 2 h at room temperature with the secondary antibody (Anti-rabbit fluorescent Alexa 594 antibody, (1:200), abcam, ab150080). Slices were acquired using a confocal laser scanning microscope (CLSM, Nikon Eclipse TE300, with the Nikon C2 scanning head), equipped with a Nikon Plan Apo 20x air objective. The setup was equipped with 488 nm and 561 nm lasers to simultaneously excite GCaMP and Alexa 594 respectively. Emission filters were 520/35 nm and 630/69 nm. For GCaMP7f⁺/PV⁺ colocalization analysis we averaged data from three slices per mouse ($n = 3$ mice).

For the evaluation of GCaMP7f expression across cortical layers in PHP.eB-injected animals, serial images were shown from three brain sections at selected distances from bregma using a Nikon Ti2-E Spinning

Disk Microscope, equipped with a CFI Plan Apo 10X Glyc numerical aperture (NA) 0.5 water immersion objective.

Statistical analysis

Imaging analysis. For comparison between groups, One- or Two-Way ANOVA was used, followed by Bonferroni test. Group-level ROI-based FC differences between pre- and post-stroke groups were assessed by means of one-way repeated measure ANOVA followed by Tukey correction. Network Based Statistic (NBS) Toolbox in MATLAB was used to statistically assess functional network connectivity [52]. We tested for both significantly higher and lower correlations. Differences were considered significant when $p < 0.05$. Errors are reported as Standard Error of Means, * $p < 0.05$, ** $p < 0.01$, *** $p < 0.001$.

Electrophysiological recordings were analyzed using Clampfit 10.7 (Molecular Devices, Sunnyvale, CA, USA), Origin 2019 (OriginLab, Northampton, MA, USA) and GraphPad Software (San Diego, CA). All data were tested for identification of outliers (ROUT, $Q = 1\%$) and for normality distribution (D'Agostino-Pearson test, GraphPad Prism 7.0) before using a linear mixed-effects model where genotype was treated as a fixed effect, and mouse and cells nested within each mouse were modeled as random effects, accounting for repeated measure within animals [53].

Behavioral test. Significant differences were tested with two-sample T-test.

Cross-correlation between Pearson Coefficient (r) and ex-vivo parameters: For each animal, the average Pearson coefficient (r) from the barrelfield cortex was correlated with the average from each electrophysiological parameter (membrane capacitance, membrane resistance, resting membrane potential, threshold, frequency, and amplitude). Linear regression analysis was performed using R. Electrophysiological parameters were modeled as a function of the Pearson Coefficient. The coefficient of determination (R^2) and p -values are reported for each comparison.

DATA AVAILABILITY

The data that support the findings of this study are available from the corresponding authors upon request.

REFERENCES

- Balasco L, Pagani M, Pangrazzi L, Chelini G, Ciancone Chama AG, Shlosman E, et al. Abnormal whisker-dependent behaviors and altered cortico-hippocampal connectivity in Shank3b^{-/-} mice. *Cereb Cortex*. 2022;32:3042–56.
- Hull JV, Dokovna LB, Jacokes ZJ, Torgerson CM, Irimia A, Van Horn JD, et al. Corrigendum: resting-state functional connectivity in autism spectrum disorders: a review. *Front Psychiatry*. 2018;9:268.
- Zerbi V, Pagani M, Markicevic M, Matteoli M, Pozzi D, Fagiolini M, et al. Correction: brain mapping across 16 autism mouse models reveals a spectrum of functional connectivity subtypes. *Mol Psychiatry*. 2022;27:3920–21.
- Nakai N, Sato M, Yamashita O, Sekine Y, Fu X, Nakai J, et al. Virtual reality-based real-time imaging reveals abnormal cortical dynamics during behavioral transitions in a mouse model of autism. *Cell Rep*. 2023;42:112258.
- Peixoto RT, Chantranupong L, Hakim R, Levasseur J, Wang W, Merchant T, et al. Abnormal striatal development underlies the early onset of behavioral deficits in Shank3B mice. *Cell Rep*. 2019;29:2016–27.e4.
- Emerson RW, Adams C, Nishino T, Hazlett HC, Wolff JJ, Zwaigenbaum L, et al. Functional neuroimaging of high-risk 6-month-old infants predicts a diagnosis of autism at 24 months of age. *Sci Transl Med*. 2017;9:eaag2882.
- Finn ES, Scheinost D, Finn DM, Shen X, Papademetris X, Constable RT. Can brain state be manipulated to emphasize individual differences in functional connectivity? *Neuroimage*. 2017;160:140–51.
- Stitt I, Hollensteiner KJ, Galindo-Leon E, Pieper F, Fiedler E, Stieglitz T, et al. Dynamic reconfiguration of cortical functional connectivity across brain states. *Sci Rep*. 2017;7:8797.
- Paasonen J, Stenroos P, Salo RA, Kiviniemi V, Gröhn O. Functional connectivity under six anesthesia protocols and the awake condition in rat brain. *Neuroimage*. 2018;172:9–20.
- Jonckers E, Shah D, Hamaide J, Verhoye M, Van der Linden A. The power of using functional fMRI on small rodents to study brain pharmacology and disease. *Front Pharmacol*. 2015;6:231.
- Lambers H, Wachsmuth L, Lippe C, Faber C. The impact of vasomotion on analysis of rodent fMRI data. *Front Neurosci*. 2023;17:1064000.
- Tsurugizawa T, Tamada K, Ono N, Karakawa S, Kodama Y, Debacker C, et al. Awake functional MRI detects neural circuit dysfunction in a mouse model of autism. *Sci Adv*. 2020;6:eaav4520.
- Mandino F, Vujic S, Grandjean J, Lake EMR. Where do we stand on fMRI in awake mice? *Cereb Cortex*. 2024;34:bhad478.
- Montagni E, Resta F, Tort-Colet N, Scaglione A, Mazzamuto G, Dextexhe A, et al. Mapping brain state-dependent sensory responses across the mouse cortex. *iScience*. 2024;27:109692.
- Scaglione A, Resta F, Goretti F, Pavone FS. Group ICA of wide-field calcium imaging data reveals the retrosplenial cortex as a major contributor to cortical activity during anesthesia. *Front Cell Neurosci*. 2024;18:1258793.
- Nietz AK, Popa LS, Streng ML, Carter RE, Kodandaramiah SB, Ebner TJ. Wide-field calcium imaging of neuronal network dynamics in vivo. *Biology*. 2022;11:1601.
- Resta F, Montagni E, de Vito G, Scaglione A, Allegra Mascaro AL, Pavone FS. Large-scale all-optical dissection of motor cortex connectivity shows a segregated organization of mouse forelimb representations. *Cell Rep*. 2022;41:111627.
- Montagni E, Resta F, Conti E, Scaglione A, Pasquini M, Micera S, et al. Wide-field imaging of cortical neuronal activity with red-shifted functional indicators during motor task execution. *J Phys D Appl Phys*. 2018;52:074001.
- Chung C, Shin W, Kim E. Early and late corrections in mouse models of autism spectrum disorder. *Biol Psychiatry*. 2022;91:934–44.
- Costales JL, Kolevzon A. Phelan-mcDermid syndrome and SHANK3: implications for treatment. *Neurotherapeutics*. 2015;12:620–30.
- De Rubeis S, Siper PM, Durkin A, Weissman J, Muratet F, Halpern D, et al. Delineation of the genetic and clinical spectrum of phelan-mcDermid syndrome caused by point mutations. *Mol Autism*. 2018;9:31.
- Monteiro P, Feng G. SHANK proteins: roles at the synapse and in autism spectrum disorder. *Nat Rev Neurosci*. 2017;18:147–57.
- Peça J, Feliciano C, Ting JT, Wang W, Wells MF, Venkatraman TN, et al. Shank3 mutant mice display autistic-like behaviours and striatal dysfunction. *Nature*. 2011;472:437–42.
- Orefice LL, Mosko JR, Morency DT, Wells MF, Tasnim A, Mozeika SM, et al. Targeting peripheral somatosensory neurons to improve tactile-related phenotypes in ASD models. *Cell*. 2019;178:867–86.e24.
- Liu J, Ye J, Ji C, Ren W, He Y, Xu F, et al. Mapping the behavioral signatures of Shank3b mice in both sexes. *Neurosci Bull*. 2024;40:1299–314.
- Michelson NJ, Vanni MP, Murphy TH. Comparison between transgenic and AAV-PHP.eB-mediated expression of GCaMP6s using wide-field functional imaging of brain activity. *Neurophotonics*. 2019;6:025014.
- Chan KY, Jang MJ, Yoo BB, Greenbaum A, Ravi N, Wu WL, et al. Engineered AAVs for efficient noninvasive gene delivery to the central and peripheral nervous systems. *Nat Neurosci*. 2017;20:1172–9.
- Fox MD, Zhang D, Snyder AZ, Raichle ME. The global signal and observed anticorrelated resting state brain networks. *J Neurophysiol*. 2009;101:3270–83.
- Li J, Kong R, Liégeois R, Orban C, Tan Y, Sun N, et al. Global signal regression strengthens association between resting-state functional connectivity and behavior. *Neuroimage*. 2019;196:126–41.
- O'Connor D, Mandino F, Shen X, Horien C, Ge X, Herman P, et al. Functional network properties derived from wide-field calcium imaging differ with wakefulness and across cell type. *Neuroimage*. 2022;264:1053–8119.
- Pagani M, Bertero A, Liska A, Galbusera A, Sabbioni M, Barsotti N, et al. Deletion of autism risk gene Shank3 disrupts prefrontal connectivity. *J Neurosci*. 2022;39:5299.
- Michelson NJ, Vanni MP, Murphy TH. Comparison between transgenic and AAV-PHP.eB-mediated expression of GCaMP6s using in vivo wide-field functional imaging of brain activity. *Neurophotonics*. 2019;6:025014.
- Mathiesen SN, Lock JL, Schoderboeck L, Abraham WC, Hughes SM. CNS transduction benefits of AAV-PHP.eB over AAV9 are dependent on administration route and mouse strain. *Mol Ther Methods Clin Dev*. 2020;19:447–58.
- Grødem S, Nymoen I, Vatne GH, Rogge FS, Bjørnsdóttir V, Lensjø KK, et al. An updated suite of viral vectors for in vivo calcium imaging using intracerebral and retro-orbital injections in male mice. *Nat Commun*. 2023;14:608.
- Jaramillo TC, Speed HE, Xuan Z, Reimers JM, Escamilla CO, Weaver TP, et al. Novel Shank3 mutant exhibits behaviors with face validity for autism and altered striatal and hippocampal function. *Autism Res*. 2017;10:42–65.
- Rahn RM, Brier LM, Bice AR, Reisman MD, Dougherty J, Culver JP. Functional connectivity of the developing mouse cortex. *Cereb Cortex*. 2021;32:1755–68.
- Malara M, Lutz A-K, Incearp B, Bauer HF, Cursano S, Volbracht K, et al. SHANK3 deficiency leads to myelin defects in the central and peripheral nervous system. *Cell Mol Life Sci*. 2022;79:371.
- Fotiadis P, Cieslak M, He X, Caciagli L, Ouellet M, Satterthwaite TD, et al. Myelination and excitation-inhibition balance synergistically shape structure-function coupling across the human cortex. *Nat Commun*. 2023;14:6115.
- Rasero J, Jimenez-Marin A, Diez I, Toro R, Hasan MT, Cortes JM. The neurogenetics of functional connectivity alterations in autism: insights from subtyping in 657 individuals. *Biol Psychiatry*. 2023;94:804–13.
- Malya AP, Wang HD, Lee HNR, Deutch AY. Microglial pruning of synapses in the prefrontal cortex during adolescence. *Cereb Cortex*. 2019;29:1634–43.

41. Dille Y, Lagae L, Swillen A, Buggenhout GV. Neurodevelopmental profile and stages of regression in phelan-mcDermid syndrome. *Dev Med Child Neurol.* 2023;65:917–25.
42. Reiersen G, Bernstein J, Froehlich-Santino W, Urban A, Purmann C, Berquist S, et al. Characterizing regression in phelan mcDermid syndrome (22q13 deletion syndrome). *J Psychiatr Res.* 2017;91:139–44.
43. Wang D, Zhou Y, Zhuo C, Qin W, Zhu J, Liu H, et al. Altered functional connectivity of the cingulate subregions in schizophrenia. *Transl Psychiatry.* 2015;5:e575–e57.
44. Bharioke A, Munz M, Brignall A, Kosche G, Eizinger MF, Ledergerber N, et al. General anesthesia globally synchronizes activity selectively in layer 5 cortical pyramidal neurons. *Neuron.* 2022;110:2024–40.
45. Murphy K, Fox MD. Towards a consensus regarding global signal regression for resting state functional connectivity MRI. *Neuroimage.* 2017;154:169–73.
46. Gotts SJ, Saad ZS, Jo HJ, Wallace GL, Cox RW, Martin A. The Perils of Global Signal Regression for Group Comparisons: A Case Study of Autism Spectrum Disorders. *Front Hum Neurosci.* 2013;7:356.
47. Maximo JO, Nelson CM, Kana RK. Unrest while resting? brain entropy in autism spectrum disorder. *Brain Res.* 2021;1762:147435.
48. Di Martino A, Fair DA, Kelly C, Satterthwaite TD, Castellanos FX, Thomason ME, et al. Unraveling the miswired connectome: a developmental perspective. *Neuron.* 2014;83:1335–53.
49. Supekar K, Musen M, Menon V. Development of large-scale functional brain networks in children. *PLoS Biol.* 2009;7:e1000157.
50. Fair DA, Cohen AL, Power JD, Dosenbach NUF, Church JA, et al. Functional brain networks develop from a “Local to Distributed” organization. *PLoS Comput Biol.* 2019;5:e1000381.
51. Scott BB, Thiberge SY, Guo C, Tervo DGR, Brody CD, Karpova AY, et al. Imaging cortical dynamics in GCaMP transgenic rats with a head-mounted widefield microscope. *Neuron.* 2018;100:1045–58.e5.
52. Zalesky A, Fornito A, Bullmore ET. Network-based statistic: identifying differences in brain networks. *Neuroimage.* 2010;53:1197–207.
53. Yu Z, Guindani M, Grieco SF, Chen L, Holmes TC, Xu X. Beyond T test and ANOVA: applications of mixed-effects models for more rigorous statistical analysis in neuroscience research. *Neuron.* 2022;110:21–35.

ACKNOWLEDGEMENTS

This work was funded by the Telethon Seed Grant for Spring 2022 (PHEM, GSA22E006), the Italian Ministry of Universities and Research PRIN 2022 (2022YCTLPL), and the THE Tuscany Health Ecosystem Project (ECS_0000017 MUR_ PNRR). Additional support was provided by Banca d'Italia and Fondo di Beneficenza di Intesa Sanpaolo through the RICONFIN Project (B/2021/0202), as well as the Fondazione Cassa di Risparmio di Firenze (CRF2020). Furthermore, this project benefited from the framework of Eurobioimaging (ESFRI research infrastructure) - Advanced Light Microscopy Italian Node.

AUTHOR CONTRIBUTIONS

ALAM conceived the study. ALAM, LB, EM supervised the project. ALAM, EM designed and interpreted experiment and computational analyses. EM, MA, AMar, LC, FP performed experiments, obtained tissue samples and generated data. EM and LC conducted computational analyses. EM, ALAM drafted the manuscript. MA, LC, AMas, LB edited the manuscript. ALAM, FSP, AMas, GM contributed funding and resources. All authors participated in the review of the manuscript.

COMPETING INTERESTS

The authors declare no competing interests.

ADDITIONAL INFORMATION

Supplementary information The online version contains supplementary material available at <https://doi.org/10.1038/s41398-025-03377-5>.

Correspondence and requests for materials should be addressed to Elena Montagni or Anna Letizia Allegra Mascaro.

Reprints and permission information is available at <http://www.nature.com/reprints>

Publisher's note Springer Nature remains neutral with regard to jurisdictional claims in published maps and institutional affiliations.



Open Access This article is licensed under a Creative Commons Attribution-NonCommercial-NoDerivatives 4.0 International License, which permits any non-commercial use, sharing, distribution and reproduction in any medium or format, as long as you give appropriate credit to the original author(s) and the source, provide a link to the Creative Commons licence, and indicate if you modified the licensed material. You do not have permission under this licence to share adapted material derived from this article or parts of it. The images or other third party material in this article are included in the article's Creative Commons licence, unless indicated otherwise in a credit line to the material. If material is not included in the article's Creative Commons licence and your intended use is not permitted by statutory regulation or exceeds the permitted use, you will need to obtain permission directly from the copyright holder. To view a copy of this licence, visit <http://creativecommons.org/licenses/by-nc-nd/4.0/>.

© The Author(s) 2025